



Cite this: *Nanoscale*, 2018, **10**, 5581

## Lower ammoniation activation energy of CoN nanosheets by Mn doping with superior energy storage performance for secondary ion batteries†

Lin Zhu, Ziliang Chen, Yun Song,\* Pei Wang, Yingchang Jiang, Le Jiang, Yong-Ning Zhou  and Linfeng Hu \*

Cationic doping has been regarded as an effective strategy to improve the electrochemical performance of transition metal composites for lithium ion batteries (LIBs). Herein, we report manganese doped cobalt nitrides ( $\text{Mn}_{0.33}\text{Co}_{0.67}\text{N}$ ) as a novel anode material for LIBs with a high reversible capacity close to  $900 \text{ mA h g}^{-1}$  after 150 cycles at a current density of  $0.5 \text{ A g}^{-1}$ , which is superior to  $749 \text{ mA h g}^{-1}$  of undoped CoN. The most fascinating performance of  $\text{Mn}_{0.33}\text{Co}_{0.67}\text{N}$  is the rate capability, in which 91% of capacity is maintained when the current density increases ten-fold from  $0.2 \text{ A g}^{-1}$  to  $2.0 \text{ A g}^{-1}$ . This enhanced electrochemical performance is attributed to the fact that Mn doping makes it faster to regenerate Co–N bonds, as evidenced by a calculated apparent ammoniation activation energy ( $E_a$ ) decrease from  $113 \text{ kJ mol}^{-1}$  to  $96 \text{ kJ mol}^{-1}$ . This fast regeneration of Co–N bonds upon conversion reactions is believed to prevent the nitride electrode from a partial loss of charge capacity upon high rate cycling, in turn facilitating the extrinsic pseudocapacitive contribution.

Received 29th November 2017,  
Accepted 17th February 2018

DOI: 10.1039/c7nr08893k

rsc.li/nanoscale

## 1. Introduction

Cobalt nitrides (CoN and  $\text{Co}_3\text{N}$ ) have been investigated as promising anode materials for lithium ion batteries (LIBs) due to their high theoretical capacity.<sup>1–3</sup> As compared with  $\text{Co}_3\text{N}$  ( $421 \text{ mA h g}^{-1}$ ), CoN exhibits a much higher reversible specific capacity of  $1102 \text{ mA h g}^{-1}$  because of the high valence (+3) of Co in CoN.<sup>4,5</sup> The electrochemical reaction of CoN is shown in eqn (1): the crystal structure destruction occurs followed by the formation of the Co–metal and  $\text{Li}_3\text{N}$  when CoN is discharged (eqn (1)), and the regeneration of CoN occurs when charged to 3.0 V (reverse reaction of eqn (1)).<sup>6,7</sup>



It can be seen from eqn (1) that the discharge process of CoN can be facilitated by continuous formation of  $\text{Li}_3\text{N}$  and Co due the high ionic conductivity of the produced  $\text{Li}_3\text{N}$  ( $6 \times 10^{-3} \text{ S cm}^{-1}$ ) and the high electrical conductivity of metal Co. However, the full and fast recharge back to CoN is still hardly achieved, which eventually leads to a gradual deterioration in reversible lithium ion storage, especially at a high rate current

density. A reasonable explanation to this problem is that the interdiffusion between the  $\text{Li}_3\text{N}$  and the Co is hindered by the segregation of these phases with the prolonged cycling, and further sluggish kinetics of the formation of Co–N bonds. This explanation is further supported by the CoN nanoparticle ( $\sim 30 \text{ nm}$ ) with a high specific capacity of  $790 \text{ mA h g}^{-1}$  at a current density of  $0.25 \text{ A g}^{-1}$  up to 25 cycles, which would be remarkably enhanced once the cycled materials are decreased to nanoscale.<sup>1</sup> Nevertheless, capacity fading of this CoN nanoparticle is noticed with a gradually decreased capacity of  $660 \text{ mA h g}^{-1}$  at the end of the 60<sup>th</sup> cycle.<sup>1</sup> It is obvious that the problem is only mediated temporarily as the newly formed Co and  $\text{Li}_3\text{N}$  domains would inevitably aggregate again upon the following cycling. Thus, to improve the high rate performance of CoN, the critical step lies in inhibiting the aggregation of the Co and  $\text{Li}_3\text{N}$  nanoparticle-based structure upon cycling and eventually improving the kinetics for the formation of Co–N bonds.

The incorporation of other metals and tuning the molar ratio of different metals could further change the electronic conductivity and promote the synergistic effects of different metal combinations, leading to a boost in the electrochemical performance. Currently, transition metal (TM = Fe, Co, Ni, Mn, etc.) doping has been employed as a catalyst to boost the electrochemical reaction kinetics, and inhibit the phase aggregation upon lithiation/de-lithiation cycles.<sup>8–11</sup> It is, therefore spontaneous to speculate on much better lithium ion storage

Department of Materials Science, Fudan University, Shanghai 200433, P. R. China.

E-mail: songyun@fudan.edu.cn, linfenghu@fudan.edu.cn

† Electronic supplementary information (ESI) available. See DOI: 10.1039/c7nr08893k

on doping the transition metal into the CoN system. Unfortunately, such attempt has failed in the Ni doped  $\text{Ni}_{0.33}\text{Co}_{0.67}\text{N}$  system, in which the capacity decreased to only ~65% of the undoped CoN at the end of the 40<sup>th</sup> cycle. This result has indicated that Ni doping has no positive effect on improving the lithium ion storage of CoN.<sup>12</sup> This may be ascribed to the larger electronegativity of Ni (1.92) than that of Co (1.88), where the stronger electronegativity of Ni than Co induces a partial electron transfer from N to Ni and thus interferes with the formation of Co–N bonds. Thus, one may imagine that if a much lower electronegativity TM, such as Mn (1.55), is introduced/doped into a CoN system, a much effective role will be played in boosting the Co–N formation, which led us to consider the same. In addition to the lower electronegativity, Mn has additional advantages: (i) it has been reported that Mn improved the structure stability and inhibited the crystallization of the  $\text{TiO}_2$  nanosheet-based structure during calcination;<sup>10</sup> (ii) known that the rate capability is one of the key indicators for lithium/sodium ion batteries (LIBs), especially for high power applications, much attention has been paid to introducing the pseudo capacitance effect into LIB systems to improve the high rate capability.<sup>13,14</sup> As compared with Ni and Fe based nitrides, MnN has shown much impressive capacitive behavior especially at high rates.<sup>2,11</sup>

Motivated by this consideration, herein, manganese doped cobalt nitrides ( $\text{Mn}_{0.33}\text{Co}_{0.67}\text{N}$ ) have been synthesized through a vapor transformation method using  $\text{MnCo}_2$ -hydroxide as the precursor. The content of Mn is about 0.33 in the compound. This is because of the use of 1/3 ratio of two transition metals in binary hydroxides and is optimal for the formation of a stable structure with high purity and crystallinity.<sup>15,16</sup> As expected,  $\text{Mn}_{0.33}\text{Co}_{0.67}\text{N}$  exhibits a high reversible capacity close to 900 mA h  $\text{g}^{-1}$  after 150 cycles at a current density of 0.5 A  $\text{g}^{-1}$ , which is superior to 749 mA h  $\text{g}^{-1}$  of undoped CoN. This enhanced electrochemical performance is attributed to the fact that Mn doping makes it faster to regenerate Co–N bonds, as obviously confirmed by the calculated apparent ammoniation activation energy ( $E_a$ ) decrease from 113 kJ  $\text{mol}^{-1}$  to 96 kJ  $\text{mol}^{-1}$ . This fast regeneration of Co–N bonds upon conversion reactions is believed to prevent the nitride electrode from a partial loss of charge capacity upon high rate cycling, in turn facilitating the extrinsic pseudocapacitive contribution. Furthermore, when applied to sodium ion batteries (SIBs),  $\text{Mn}_{0.33}\text{Co}_{0.67}\text{N}$  electrodes exhibit a high reversible capacity over 240 mA h  $\text{g}^{-1}$  after 120 cycles at a current density of 0.5 A  $\text{g}^{-1}$ . This investigation has quantitatively revealed the mechanism on Mn doping in improving lithium the ion storage performance, paving the way for new power battery materials for commercial secondary ion batteries.

## 2. Experimental section

### 2.1. Synthesis of $\text{Mn}_{0.33}\text{Co}_{0.67}\text{N}$ nanosheets

Hexagonal  $\text{Mn}_{0.33}\text{Co}_{0.67}\text{N}$  nanosheets were synthesized by homogeneous precipitation and a further ammoniation

process. Firstly, 5 mmol of cobalt chloride ( $\text{CoCl}_2 \cdot 6\text{H}_2\text{O}$ ), 2.5 mmol of manganese chloride ( $\text{MnCl}_2$ ) and 45 mmol of hexamethylenetetramine (HMT) were dissolved in 1000  $\text{cm}^3$  of deionized water. This solution was refluxed for 6 h under continuous magnetic stirring and argon protection. The pink precipitate was recovered by filtration, washed with deionized water and anhydrous ethanol in turn, and finally air-dried at room temperature. Then,  $\text{Mn}_{0.33}\text{Co}_{0.67}\text{N}$  was obtained by thermal annealing at 270 °C for 2 h with a heating rate of 2 °C  $\text{min}^{-1}$  in the presence of  $\text{NH}_3/\text{Ar}$  gas. Hexagonal CoN nanosheets were synthesized by the same steps without the addition of  $\text{MnCl}_2$ .

### 2.2. Material characterization

Sample morphologies were characterized using a FEI Nova Nano Sem 450 field-emission scanning electron microscope (SEM), a FEI Tecnai G2 F 20 S-Twin transmission electron microscope (TEM), and a Bruker Dimension Icon atomic force microscope. The crystal structure characteristics were studied using a X-ray powder diffraction (XRD) (Bruker D8-A25 diffractometer using  $\text{Cu K}\alpha$  radiation ( $\lambda = 1.5406 \text{ \AA}$ )). The thermal behavior was determined by differential scanning calorimetry (DSC) on a Netzsch STA 409 PC. AFM images were acquired in tapping-mode using a Si tip cantilever.

### 2.3. Electrochemical measurements

To fabricate working electrodes, active powder, graphene and binder (polyvinylidene fluoride, PVdF) were mixed in a weight ratio of 70 : 20 : 10; 1-methyl-2-pyrrolidinone solvent (Aldrich, 99%) was added to form a slurry. Graphene is used to replace the traditional conductive agent Super P in our electrode preparation process. The graphene acts not only as a conductive agent, but also as a structure promoter to induce pseudo-capacitance behavior.<sup>17</sup> The optimal amount of 20 wt% graphene content shows the most favourable structure where active composites lie flat on the surface of graphene.<sup>18</sup> The well-mixed slurry was coated onto a Cu foil as a current collector using a doctor blade technique and then dried under vacuum at 70 °C for 12 h. Coin-type half-cells were assembled inside an argon-filled glove box (<5 ppm,  $\text{H}_2\text{O}$  and  $\text{O}_2$ ), using Li metal foils as counter electrodes, porous polypropylene membrane as separators, and 1.0 M  $\text{LiPF}_6$  in a mixture of ethylene carbonate and dimethyl carbonate (1 : 1) as the electrolyte. The charge–discharge cycling was performed within the voltage range of 0.01–3.0 V vs.  $\text{Li/Li}^+$  on a battery test instrument (CT2001A, LAND). Cyclic voltammetry (CV) was performed on an electrochemical workstation (CHI660e). With respect to sodium ion battery application, half-cells were assembled in an argon-filled glove box (<5 ppm,  $\text{H}_2\text{O}$  and  $\text{O}_2$ ), using the metallic sodium foil as the counter electrode, the Whatman glass fiber as the separator and 0.5 L  $\text{mol}^{-1}$   $\text{CF}_3\text{SO}_3\text{Na}$  solution in diethylene glycol dimethyl ether as the electrolyte. The charge–discharge cycling was performed within the voltage range of 0.01–2.80 V vs.  $\text{Na/Na}^+$  on a battery test instrument (CT2001A, LAND).

### 3. Results and discussion

#### 3.1. Thermal behavior and phase evolution of $\text{Mn}_{0.33}\text{Co}_{0.67}\text{N}$

The thermal behavior and phase evolution of the products during calcination are examined by DSC and XRD, as shown in Fig. 1, illustrating the patterns of  $\text{Mn}_{0.33}\text{Co}_{0.67}(\text{OH})_2$ ,  $\text{Mn}_{0.33}\text{Co}_{0.67}\text{N}$  and  $\text{MnCo}$  solid solution, respectively. The DSC curves of the as-synthesized  $\text{Mn}_{0.33}\text{Co}_{0.67}(\text{OH})_2$  precursor with increasing temperature under an  $\text{NH}_3/\text{Ar}$  atmosphere are shown in Fig. 1a. Firstly, the  $\text{Mn}_{0.33}\text{Co}_{0.67}(\text{OH})_2$  is prepared by a facile homogeneous precipitation method including refluxing a solution containing  $\text{CoCl}_2\text{-MnCl}_2\text{-HMT}$  ( $\text{Co}^{2+}/\text{Mn}^{2+}$  molar ratio of 2 : 1, HMT: hexamethylenetetramine) under a flowing  $\text{N}_2$  atmosphere. As seen from Fig. 1b, all the diffraction peaks of the  $\text{Mn}_{0.33}\text{Co}_{0.67}(\text{OH})_2$  template can be indexed to a brucite structure reported in the previous study.<sup>13</sup> This  $\text{Mn}_{0.33}\text{Co}_{0.67}(\text{OH})_2$  precursor is subjected to subsequent annealing under an  $\text{NH}_3/\text{Ar}$  atmosphere. The first endothermic peak of the DSC curve at 250 °C is related to the formation of the  $\text{Mn}_{0.33}\text{Co}_{0.67}\text{N}$  phase by ammoniation of the  $\text{Mn}_{0.33}\text{Co}_{0.67}(\text{OH})_2$  precursor, as confirmed by the XRD pattern (Fig. 1c). All diffraction peaks of the XRD pattern can be indexed to the standard JCPDS no. 73-1702 (CoN), indicating a cubic phase with the  $F\bar{4}3m$  space group.<sup>1,19,20</sup> Our previous work has demonstrated that the Co/M ( $M = \text{Ni}, \text{Fe}, \text{Mn}, \text{Cu}, \text{etc.}$ ) shows no changes of atomic ratio/arrangement during the vapour transformation from the rhombohedral hydroxide precursor (space group  $P\bar{3}m$ ) to the cubic  $\text{MCo}_2\text{O}_4$  spinel (S.G.  $Fd\bar{3}m$ ), resulting in a single-crystal structure of the as-transformed  $\text{MCo}_2\text{O}_4$  oxide.<sup>20</sup> Thus, it is reasonable that the phase can be written as  $\text{Mn}_{0.33}\text{Co}_{0.67}\text{N}$  for the fixed  $\text{Co}^{2+}/\text{Mn}^{2+}$  molar ratio.

The crystal structure of the  $F\bar{4}3m$  space group of  $\text{Mn}_{0.33}\text{Co}_{0.67}\text{N}$  can be described with Co and Mn occupying (0 0 0) and N at (1/2 1/2 1/2) with face centred translation.<sup>1,19,20</sup> The DSC result combined with the corresponding XRD analysis has demonstrated that ammoniation of the  $\text{MnCo}_2\text{-hydroxide}$  starts at 200 °C, and ends at a temperature of 270 °C with a pure  $\text{Mn}_{0.33}\text{Co}_{0.67}\text{N}$  phase with no diffraction peaks of impurity. Based on these thermal behavior and phase evolution results, 270 °C and 2 hours have been determined to realize the complete ammoniation of the  $\text{Mn}_{0.33}\text{Co}_{0.67}\text{N}$  phase. This ammoniation process involves low energy consumption, in which the temperature is 85 °C lower than 335 °C of the reaction between  $\text{Co}_3\text{O}_4$  and  $\text{NH}_3$ , as previously reported.<sup>1</sup> One interesting thing observed in the XRD comparison between CoN and  $\text{Mn}_{0.33}\text{Co}_{0.67}\text{N}$  is that the Mn doping sample shifts slightly to a lower angle, as shown in Fig. S1,† which is caused by the larger radius of  $\text{Mn}^{2+}/\text{Mn}^{3+}$  (73 pm/67 pm), as compared with that of  $\text{Co}^{3+}$  (61 pm). This slight angle shift is further confirmed by the Rietveld refinement analysis, as shown in Fig. S2.† The  $\text{Mn}_{0.33}\text{Co}_{0.67}\text{N}$  crystallized in the cubic  $F\bar{4}3m$  structure, with lattice parameters  $a = b = c = 4.267 \text{ \AA}$ , while CoN in the cubic  $F\bar{4}3m$  structure, with lattice parameters  $a = b = c = 4.253 \text{ \AA}$ . On further increasing the annealing temperature to above 544 °C, a  $\text{MnCo}_2$  solid solution is obtained, as confirmed in the XRD pattern (Fig. 1d). According to above discussion, we can conclude the general ammoniation reactions for the phase evolution under  $\text{NH}_3/\text{Ar}$  as follows:

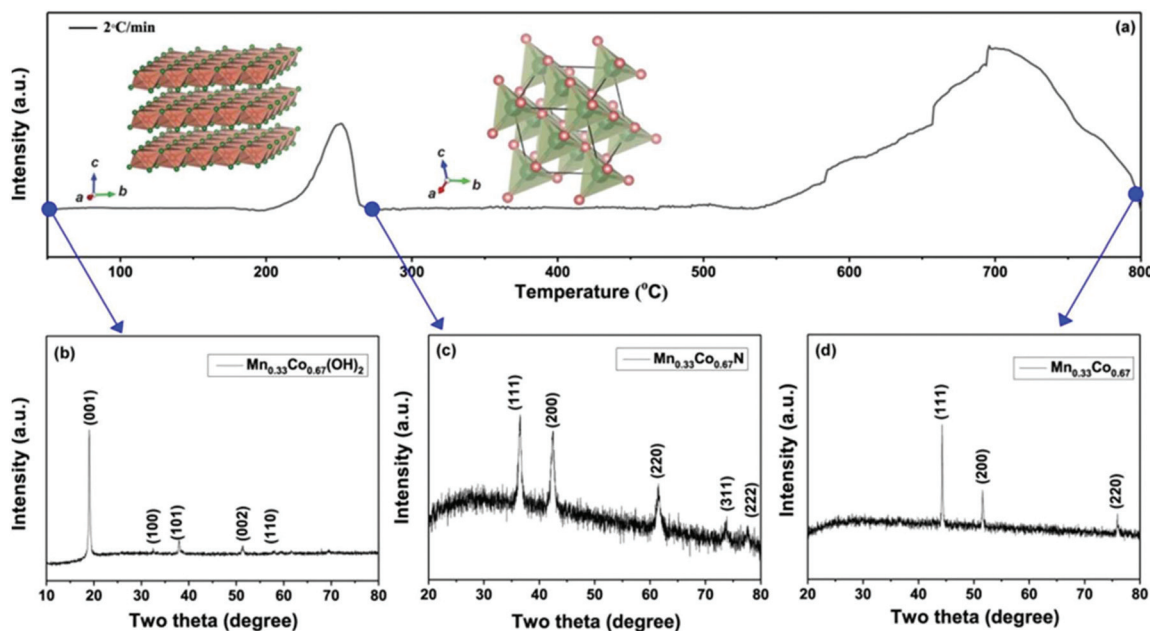
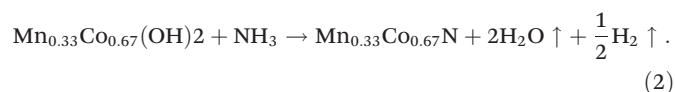


Fig. 1 (a) Thermal behavior and (b–d) phase evolution of the products during ammoniation.

### 3.2. Morphology and structure of $\text{Mn}_{0.33}\text{Co}_{0.67}\text{N}$

The SEM image of  $\text{Mn}_{0.33}\text{Co}_{0.67}\text{N}$  in Fig. 2a shows large amounts of regular hexagonal nanosheets. An individual  $\text{Mn}_{0.33}\text{Co}_{0.67}\text{N}$  sheet, for which the lateral length is 2  $\mu\text{m}$ , is shown in Fig. 2b. The atomic force microscopy (AFM) image in Fig. 2c shows a 2D hexagonal nanosheet with a relatively smooth surface similar to those observed in the SEM image. The height profile in the AFM image reveals that the nanosheet has an average thickness of  $\sim 50$  nm. As seen from Fig. 2d–f, the uniform distribution of Mn, Co and N elements of the nanosheet can be further confirmed by the energy-dispersive X-ray (EDX) spectra mapping images. It should be noted here that Mn doping does not change the morphology of CoN, as shown in Fig. S3,<sup>†</sup> showing similar hexagonal nanosheets to that of the  $\text{Mn}_{0.33}\text{Co}_{0.67}\text{N}$ .

The pristine  $\text{Mn}_{0.33}\text{Co}_{0.67}(\text{OH})_2$  shows a well-developed 2D nanosheet morphology with a regular hexagonal frame, sharp corners and smooth surface, as shown in Fig. S4.<sup>†</sup> The selected area electron diffraction (SAED) patterns taken from an individual hydroxide nanosheet display sharp hexagonally

arranged diffraction spots, as shown in Fig. S4,<sup>†</sup> demonstrating that each  $\text{Mn}_{0.33}\text{Co}_{0.67}(\text{OH})_2$  nanosheet is highly crystallized with a single-crystal nature. After ammoniation, the regular hexagonal morphology of  $\text{Mn}_{0.33}\text{Co}_{0.67}\text{N}$  is maintained, as shown in the TEM image in Fig. 2g. Moreover, the surface of ammoniation products is rather rough, indicating that the nanosheets are rendered porous on heating. The selected-area electron diffraction (SAED) pattern taken from an individual porous  $\text{Mn}_{0.33}\text{Co}_{0.67}\text{N}$  hexagonal nanosheet shows Debye–Scherrer rings combined with some diffraction spots, as shown in Fig. 2h. Such a pattern is characteristic of a mosaic structure composed of a large number of small crystalline domains which are slightly misaligned with respect to each other, and usually observed in the as-transformed oxide from their hydroxide precursor. The SAED pattern of  $\text{Mn}_{0.33}\text{Co}_{0.67}\text{N}$  can be indexed to the (111), (200) and (220) planes of cubic  $\text{Mn}_{0.33}\text{Co}_{0.67}\text{N}$  starting from the inner to the outer ring, respectively. The diffused rings also suggest that the sheets are no more single crystalline like the precursor hydroxide sheets. In the corresponding High Resolution TEM (HRTEM) image, as shown in Fig. 2i, the lattice fringe is clearly observed, and at

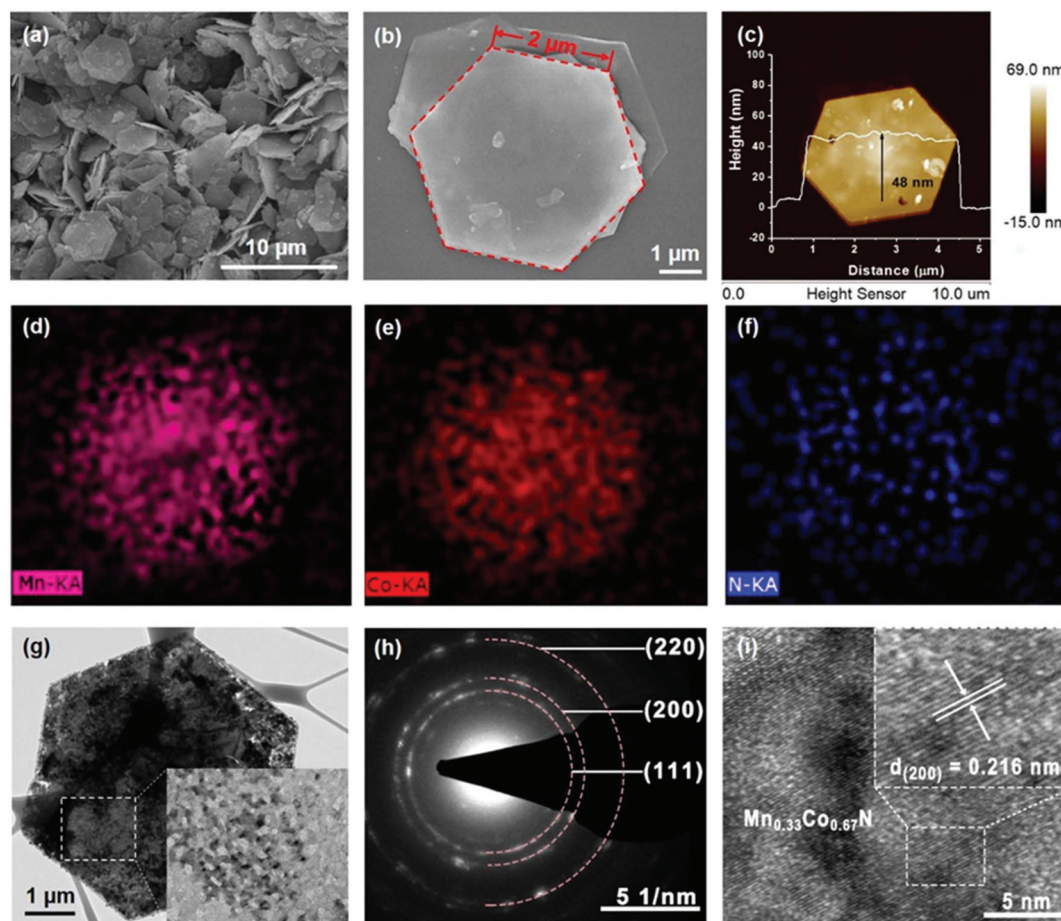


**Fig. 2** (a) The SEM image of  $\text{Mn}_{0.33}\text{Co}_{0.67}\text{N}$  nanosheets; (b) an individual  $\text{Mn}_{0.33}\text{Co}_{0.67}\text{N}$  sheet; (c) tapping-mode AFM image of the  $\text{Mn}_{0.33}\text{Co}_{0.67}\text{N}$  nanosheets deposited on a Si wafer, inset is the height profile along the surface; (d–f) corresponding EDX elemental mapping image of Mn, Co, N elements; (g) typical TEM image, (h) diffraction pattern and (i) high-resolution TEM image of  $\text{Mn}_{0.33}\text{Co}_{0.67}\text{N}$  nanosheets.

a spacing that corresponded closely to the (200) plane of the cubic  $\text{Mn}_{0.33}\text{Co}_{0.67}\text{N}$ .

### 3.3. The role of Mn in $\text{Mn}_{0.33}\text{Co}_{0.67}\text{N}$ formation

The  $\text{Mn}_{0.33}\text{Co}_{0.67}\text{N}$  or CoN can be prepared by a general solid-gas reaction, which can be conducted in three steps, as shown in Fig. 3a: (i) physical adsorption of  $\text{NH}_3$  molecules on the surface of  $\text{Mn}_{0.33}\text{Co}_{0.67}(\text{OH})_2$  or  $\text{Co}(\text{OH})_2$  nanosheets and then dissociated into N and H atoms, (ii) diffusion of N atoms driven by the significant concentration difference, and (iii) formation of Co–N bonds.<sup>21–23</sup> The kinetics of first two steps mainly depend on the surface morphology and thickness of the  $\text{Mn}_{0.33}\text{Co}_{0.67}\text{N}$  and CoN. Given a similar morphology of  $\text{Mn}_{0.33}\text{Co}_{0.67}\text{N}$  and CoN, it can be deduced that the difference in the ammoniation rate between  $\text{Mn}_{0.33}\text{Co}_{0.67}\text{N}$  and CoN leads the formation of Co–N bonds.

To quantitatively elucidate the role of Mn doping in the formation of Co–N bonds, the apparent ammoniation activation energies ( $E_a$ ) for  $\text{Mn}_{0.33}\text{Co}_{0.67}(\text{OH})_2$  and  $\text{Co}(\text{OH})_2$  are determined using the Kissinger's approach:<sup>18,19</sup>

$$\frac{d \ln \left( \frac{\beta}{T_m^2} \right)}{d \left( \frac{1}{T_m} \right)} = -\frac{E_a}{R} \quad (3)$$

where  $\beta$ ,  $T_m$  and  $R$  are the heating rate, the absolute temperature for the maximum ammoniation rate, and the gas constant, respectively. In this study,  $T_m$  can be obtained from DSC curves at the heating rates of 1, 2, 4, and 5 °C  $\text{min}^{-1}$ , as shown in Fig. 3b and c for the  $\text{Mn}_{0.33}\text{Co}_{0.67}(\text{OH})_2$  and  $\text{Co}(\text{OH})_2$ ,

respectively. The dependences of  $\ln(\beta/T_m^2)$  on  $1/T_m$  are plotted in Fig. 3d, by fitting the data, the ammoniation activation energies for the  $\text{Mn}_{0.33}\text{Co}_{0.67}(\text{OH})_2$  and  $\text{Co}(\text{OH})_2$  are determined to be 113  $\text{kJ mol}^{-1}$  and 96  $\text{kJ mol}^{-1}$ , respectively. The decreased  $E_a$  from 113  $\text{kJ mol}^{-1}$  and 96  $\text{kJ mol}^{-1}$  gives a strong proof that Mn doping boosts the formation kinetics of Co–N bonds. This may be ascribed to the weak electronegativity of Mn (1.55) compared to that of Co (1.88), in which Mn will provide electrons to N easily, and facilitate the Co–N formation.<sup>24</sup> From the above results, thermal behavior and morphology analysis, the effect of Mn doping in CoN can be summarized as: (i) expands the lattice parameters of CoN, because the radius of  $\text{Mn}^{2+}/\text{Mn}^{3+}$  (73 pm/67 pm) is larger than that (61 pm) of  $\text{Co}^{3+}$ ; (ii) boosts the formation kinetics of Co–N bonds, decreasing the ammoniation  $E_a$  from 113  $\text{kJ mol}^{-1}$  and 96  $\text{kJ mol}^{-1}$ . It is believed that these aspects have a positive effect on lithium ion storage performance.

### 3.4. Lithium ion storage performance of $\text{Mn}_{0.33}\text{Co}_{0.67}\text{N}$

The lithium ion storage properties of the  $\text{Mn}_{0.33}\text{Co}_{0.67}\text{N}$  and CoN nanosheets are compared in coin cells with Li foil as the counter electrode. It should be mentioned here that graphene is employed to replace the traditional conductive carbon (Super P) as a conductive agent in our electrode preparation. All the current densities and specific capacities presented are calculated based on the mass of active CoN and  $\text{Mn}_{0.33}\text{Co}_{0.67}\text{N}$ . This electrode preparation has been proved to be effective and suitable, especially for two dimensional nanosheets, in which nanosheets were in contact with the graphene matrix face-to-face.<sup>13,14</sup>

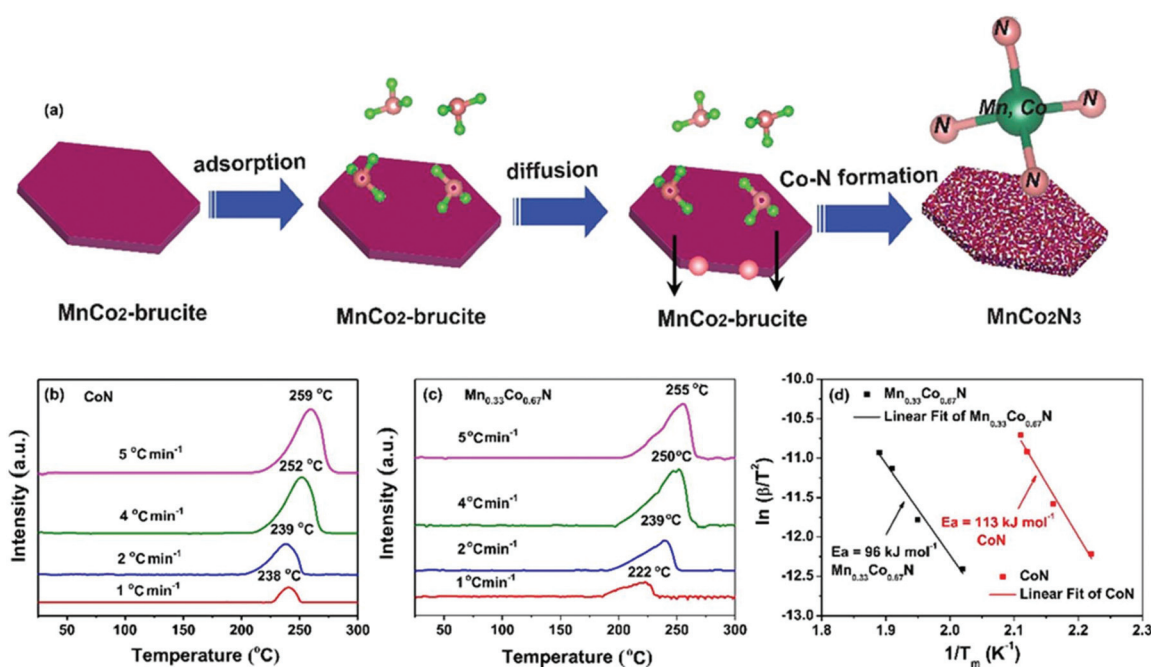
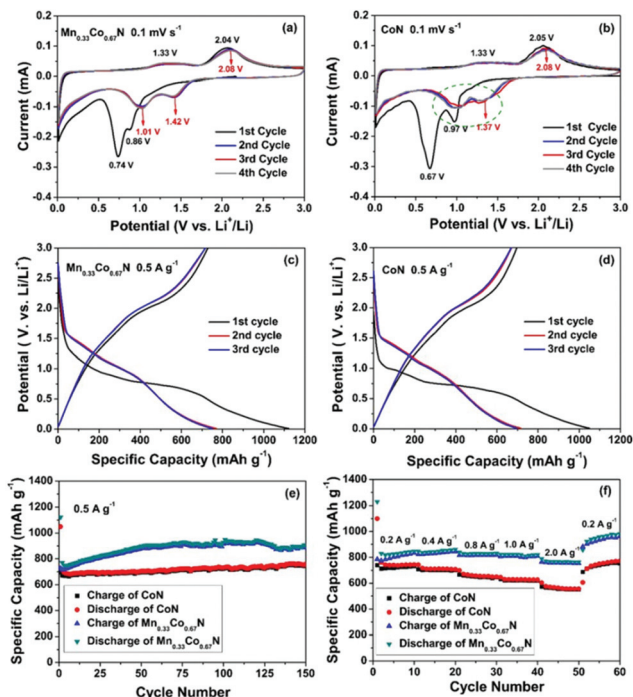


Fig. 3 (a) Illustration of the dynamic evolution process of the  $\text{Mn}_{0.33}\text{Co}_{0.67}\text{N}$  polycrystalline nanosheet. DSC curves of ammoniation of (b)  $\text{Co}(\text{OH})_2$  and (c)  $\text{Mn}_{0.33}\text{Co}_{0.67}(\text{OH})_2$  at heating rates of 1–5 °C  $\text{min}^{-1}$ , and (d) Kissinger's plots of CoN and  $\text{Mn}_{0.33}\text{Co}_{0.67}\text{N}$ , respectively.



**Fig. 4** (a) and (b) Representative CV curve of the  $\text{Mn}_{0.33}\text{Co}_{0.67}\text{N}$  and  $\text{CoN}$  for the first to the fourth cycles at a scan rate of  $0.1 \text{ mV s}^{-1}$ , respectively; (c) and (d) galvanostatic charge–discharge voltage profiles of the  $\text{Mn}_{0.33}\text{Co}_{0.67}\text{N}$  and  $\text{CoN}$  at a current density of  $0.5 \text{ A g}^{-1}$ , respectively; (e) comparative cycling performance of  $\text{Mn}_{0.33}\text{Co}_{0.67}\text{N}$  and  $\text{CoN}$  at a current density of  $0.5 \text{ A g}^{-1}$ ; (f) rate properties of the  $\text{Mn}_{0.33}\text{Co}_{0.67}\text{N}$  and  $\text{CoN}$  at different current densities.

Fig. 4a shows the cyclic voltammetry (CVs) curves of the  $\text{Mn}_{0.33}\text{Co}_{0.67}\text{N}$ , which are collected at a scan rate of  $0.1 \text{ mV s}^{-1}$  for the first four cycles in a potential window of  $0.01\text{--}3.0 \text{ V}$  versus  $\text{Li}^+/\text{Li}$ . In the first cathodic process, a small cathodic peak at  $0.86 \text{ V}$  indicates an insertion process of lithium ions into the  $\text{Mn}_{0.33}\text{Co}_{0.67}\text{N}$  lattice with an initiation of crystal structure destruction. A major cathodic peak is observed at  $0.74 \text{ V}$ , which can be attributed to a multi-step electrochemical reaction process, including the formation of solid electrolyte interface (SEI) layers and the formation of the Mn/Co–metal and  $\text{Li}_3\text{N}$ .<sup>1,19</sup> In the first anodic sweep, two oxidation peaks located at  $1.33$  and  $2.04 \text{ V}$  refer to the oxidation process and reformation of corresponding metal nitrides. The second cathodic sweep differs from the first one, where the peaks at  $0.86 \text{ V}$  and  $0.74 \text{ V}$  disappear and are replaced by new bump emerges ranged from  $1.01$  to  $1.42 \text{ V}$ , which is due to the irreversible structural change of  $\text{Mn}_{0.33}\text{Co}_{0.67}\text{N}$  after the first discharge.<sup>19</sup> In the subsequent cycles, the reduction peaks and oxidation peaks overlap well with those of the second cycle, indicating an excellent reversibility of  $\text{Mn}_{0.33}\text{Co}_{0.67}\text{N}$ . Fig. 4b shows the cycling CV curves of the  $\text{CoN}$  for comparison. The electrochemical feature is similar to that of  $\text{Mn}_{0.33}\text{Co}_{0.67}\text{N}$ , meaning that the Mn doping does not change the thermodynamic properties of  $\text{CoN}$ .<sup>24,25</sup> The major difference between  $\text{Mn}_{0.33}\text{Co}_{0.67}\text{N}$  and  $\text{CoN}$  is that the cathodic bump from  $1.00$

$1.42 \text{ V}$  of  $\text{CoN}$  presents a zigzag shape (circled in green colour), whereas this cathodic bump of  $\text{Mn}_{0.33}\text{Co}_{0.67}\text{N}$  is much smoother. This phenomenon is attributed to the fact that Mn doping improves the structure stability during lithiation/delithiation cycles as previously reported for the Mn-doped  $\text{TiO}_2$  system.<sup>9</sup>

The galvanostatic discharge-charge (GDC) voltage profiles of  $\text{Mn}_{0.33}\text{Co}_{0.67}\text{N}$  and  $\text{CoN}$  in the potential window of  $0.01\text{--}3 \text{ V}$  at a current density of  $0.5 \text{ A g}^{-1}$  are compared in Fig. 4c and d, respectively. For  $\text{Mn}_{0.33}\text{Co}_{0.67}\text{N}$ , an obvious plateau around  $0.8 \text{ V}$  in the first discharge process can be attributed to a multi-step electrochemical reaction process, the formation of solid electrolyte interface (SEI) layers and the formation of the Mn/Co–metal and  $\text{Li}_3\text{N}$ . After the first cycle, the discharge/charge curves are in high coincidence, indicating a reversible and stable electrochemical performance. These GDC results are well consistent with the CV results. In the initial cycle,  $\text{Mn}_{0.33}\text{Co}_{0.67}\text{N}$  delivers a discharge capacity of  $1121 \text{ mA h g}^{-1}$  and a charge capacity of  $729 \text{ mA h g}^{-1}$ , with a low corresponding coulombic efficiency of  $65\%$ . The low coulombic efficiency in the first cycle is ascribed to the initial formation of SEI layers. To compare the electrochemical performance of  $\text{Mn}_{0.33}\text{Co}_{0.67}\text{N}$  and  $\text{CoN}$ , the GDC profile of pure  $\text{CoN}$  is shown in Fig. 4d. In the initial cycle,  $\text{CoN}$  shows a discharge capacity of  $1049 \text{ mA h g}^{-1}$  and a charge capacity of  $696 \text{ mA h g}^{-1}$ , with a coulombic efficiency of  $66\%$ . There is no obvious difference of the GDC profile between  $\text{Mn}_{0.33}\text{Co}_{0.67}\text{N}$  and  $\text{CoN}$ , except for the alleviation of voltage polarization after Mn-doping, as shown in Fig. S5 and S6.†

The cycling performance at a current density of  $0.5 \text{ A g}^{-1}$  of  $\text{Mn}_{0.33}\text{Co}_{0.67}\text{N}$  and  $\text{CoN}$  is shown in Fig. 4e. The specific capacity of  $\text{CoN}$  is stabilized at  $751 \text{ mA h g}^{-1}$  after 150 cycles, with capacity fading less than  $0.19\%$  per cycle. In contrast, the specific capacity of  $\text{Mn}_{0.33}\text{Co}_{0.67}\text{N}$  is stabilized at  $896 \text{ mA h g}^{-1}$ , with capacity fading less than  $0.13\%$  per cycle. The cycling performance at an increased current density of  $2.0 \text{ A g}^{-1}$  of  $\text{Mn}_{0.33}\text{Co}_{0.67}\text{N}$  and  $\text{CoN}$  is shown in Fig. S7,† in which the specific capacity of  $\text{Mn}_{0.33}\text{Co}_{0.67}\text{N}$  is stabilized at  $690 \text{ mA h g}^{-1}$  after 200 cycles, and higher than  $480 \text{ mA h g}^{-1}$  of  $\text{CoN}$ . The rate capability of  $\text{Mn}_{0.33}\text{Co}_{0.67}\text{N}$  and  $\text{CoN}$  electrodes in the range of  $0.01\text{--}3.00 \text{ V}$  is evaluated at various current densities ( $0.2\text{--}2.0 \text{ A g}^{-1}$ ), as shown in Fig. 4f. The  $\text{CoN}$  electrodes show only  $730, 699, 646, 620,$  and  $546 \text{ mA h g}^{-1}$  at current densities of  $0.2, 0.4, 0.8, 1.0$  and  $2.0 \text{ A g}^{-1}$ , respectively. In contrast, the  $\text{Mn}_{0.33}\text{Co}_{0.67}\text{N}$  exhibits a much higher reversible capacity of  $841, 838, 812, 807,$  and  $766 \text{ mA h g}^{-1}$  at current densities of  $0.2, 0.4, 0.8, 1.0$  and  $2.0 \text{ A g}^{-1}$ , respectively. In addition, when the current density is changed back to  $0.2 \text{ A g}^{-1}$ , the capacity of the  $\text{Mn}_{0.33}\text{Co}_{0.67}\text{N}$  returns to  $951 \text{ mA h g}^{-1}$ . This lithium ion storage performance of  $\text{Mn}_{0.33}\text{Co}_{0.67}\text{N}$  is superior to those of other as-reported metal nitrides on the basis of a comprehensive summary (Table 1). Apparently, the  $\text{Mn}_{0.33}\text{Co}_{0.67}\text{N}$  exhibits much improved cycling stability and rate capability as compared with the undoped  $\text{CoN}$ . The cycling stability of  $\text{Mn}_{0.33}\text{Co}_{0.67}\text{N}$  during lithiation/de-lithiation is due to the structure stability facilitated by Mn doping. It is demonstrated

**Table 1** Comparison of the characteristic parameters of different nitride electrodes for LIB applications

Electrodes	Current density	Cycling number	Specific Capacity	Ref.
CrN	0.028 mA cm <sup>-2</sup>	30	750 mA h g <sup>-1</sup>	26
Fe <sub>2</sub> N@C	1 A g <sup>-1</sup>		475 mA h g <sup>-1</sup>	27
	2 A g <sup>-1</sup>		450 mA h g <sup>-1</sup>	
VN	0.028 mA cm <sup>-2</sup>	50	800 mA h g <sup>-1</sup>	28
Zn <sub>3</sub> N <sub>2</sub>	23 mA g <sup>-1</sup>	1	555 mA h g <sup>-1</sup>	29
Cu <sub>3</sub> N	228 mA g <sup>-1</sup>	200	300 mA h g <sup>-1</sup>	
Ni <sub>0.33</sub> Co <sub>0.67</sub> N	0.5 A g <sup>-1</sup>	50	350 mA h g <sup>-1</sup>	30
	0.25 A g <sup>-1</sup>	50	400 mA h g <sup>-1</sup>	
Ni <sub>3</sub> N	1 Li at 20 h	10	348 mA h g <sup>-1</sup>	31
Fe <sub>3</sub> N	0.007 mA cm <sup>-2</sup>	40	500 mA h g <sup>-1</sup>	32
Co <sub>3</sub> N	0.007 mA cm <sup>-2</sup>	40	410 mA h g <sup>-1</sup>	32
CoN	250 mA g <sup>-1</sup>	80	990 mA h g <sup>-1</sup>	33
Mn <sub>3</sub> N <sub>2</sub>	80 mA g <sup>-1</sup>	110	463 mA h g <sup>-1</sup>	34
TiN	335 mA g <sup>-1</sup>	100	450 mA h g <sup>-1</sup>	35
Mo <sub>2</sub> N	0.1 mA cm <sup>-2</sup>	100	696 mA h g <sup>-1</sup>	36
Li <sub>4</sub> Ti <sub>5</sub> O <sub>12</sub> /TiN	1C	40	161 mA h g <sup>-1</sup>	37
G/TiN	20 mA g <sup>-1</sup>	200	554 mA h g <sup>-1</sup>	38
VN/GC	21 mA g <sup>-1</sup>	10	340 mA h g <sup>-1</sup>	39
TiVN/C	74.4 mA g <sup>-1</sup>	20	678 mA h g <sup>-1</sup>	40
Si/TiN	0.23 mA cm <sup>-2</sup>	20	300 mA h g <sup>-1</sup>	41
CoN	500 mA g <sup>-1</sup>	150	751 mA h g <sup>-1</sup>	This work
Mn <sub>0.33</sub> Co <sub>0.67</sub> N	500 mA g <sup>-1</sup>	150	896 mA h g <sup>-1</sup>	This work

that Mn doping does not change the thermodynamic properties of CoN, thus the improved rate capability is attributed to the enhanced kinetics of the lithiation/de-lithiation process. Moreover, the EIS analysis has been performed, as shown in Fig. S8,† to further confirm the effect of Mn-doping. The Nyquist plots consist of depressed semi-circles and inclined lines. The semi-circle observed in the high and middle frequency range corresponds to the charge transfer resistance ( $R_{ct}$ ) at the interface of the electrodes. After simulating the semi-circles of two samples using the equivalent circuit, the values of  $R_{ct}$  of Mn<sub>0.33</sub>Co<sub>0.67</sub>N and pure CoN are calculated to be 30.65 and 35.1  $\Omega$ , respectively. The smaller  $R_{ct}$  of Mn<sub>0.33</sub>Co<sub>0.67</sub>N indicates that the electron transportation inside Mn<sub>0.33</sub>Co<sub>0.67</sub>N is faster than that of pure CoN. The lithium diffusion coefficients of Mn<sub>0.33</sub>Co<sub>0.67</sub>N and pure CoN are determined to be  $1.46 \times 10^{-14}$  and  $2.82 \times 10^{-15}$  cm<sup>2</sup> s<sup>-1</sup>, respectively. This result clearly suggests that Li ion diffusion is facilitated in Mn<sub>0.33</sub>Co<sub>0.67</sub>N compared with pure CoN.

### 3.5. The role of Mn in lithiation/de-lithiation kinetics

To answer the question that what role does Mn doping plays in lithiation/de-lithiation kinetics, quantitative analysis such as cyclic voltammetry (CV) at different scan rates is performed. Fig. 5a and b show the cyclic voltammograms of the electrode after 100 cycles at different scan rates from 0.1 to 0.9 mV s<sup>-1</sup> for Mn<sub>0.33</sub>Co<sub>0.67</sub>N and pure CoN, respectively. The current intensity increases along with the increase of the scan rate for both Mn<sub>0.33</sub>Co<sub>0.67</sub>N and pure CoN samples. In addition, the peaks in the CV curves show a relatively little change in potential as a function of the sweep rate, which is indicative of fast charge transfer processes. It has been reported that the lithium storage mechanism (a diffusion-controlled electro-

chemical reaction or a capacitive process) could be estimated according to the following equations:<sup>42</sup>

$$i = av^b \quad (4)$$

$$\log(i) = b \times \log(v) + \log(a) \quad (5)$$

where  $i$  is the current,  $v$  is the scan rate, and  $a$  and  $b$  are adjustable parameters. When the  $b$ -value approaches 1.0, the kinetics are controlled by the capacitive process (extrinsic pseudo-capacitance effect), and when the  $b$ -value is close to 0.5, the kinetics are diffusion-controlled (conversion and alloying reactions). If the  $b$ -value is between 0.5 and 1.0, the process is controlled by the synergic effect of the electrochemical process and capacitive process. Fig. 5b and c show the  $\log i$  vs.  $\log v$  plots of the Mn<sub>0.33</sub>Co<sub>0.67</sub>N and pure CoN electrodes. The calculated  $b$ -values of the CoN electrode are 0.90, 0.86 and 0.85 at

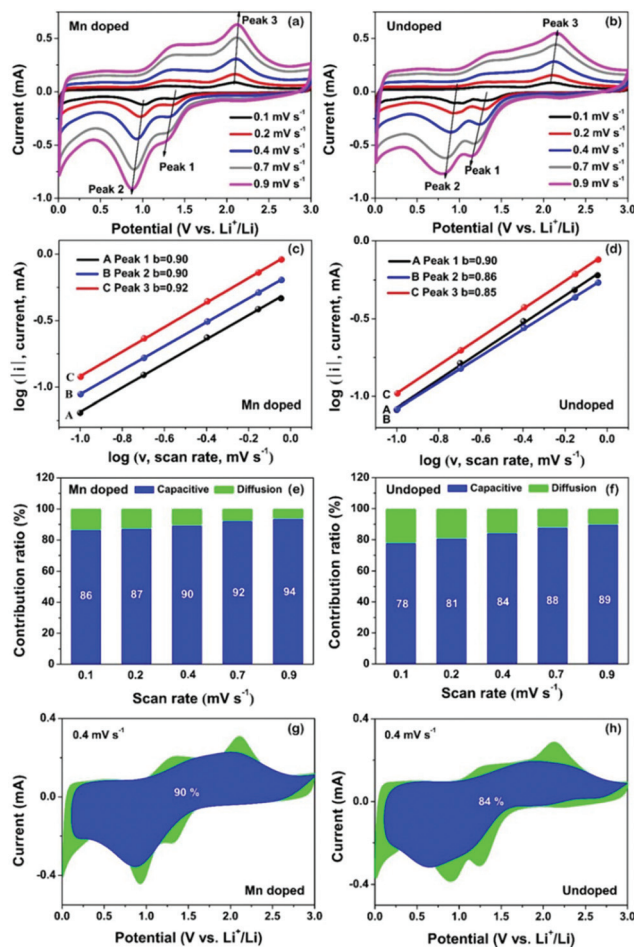


**Fig. 5** (a) and (b) Show the cyclic voltammograms of the electrode after 100 cycles at different scan rates from 0.1 to 0.9 mV s<sup>-1</sup> for Mn<sub>0.33</sub>Co<sub>0.67</sub>N and CoN, respectively; (c) and (d) show  $\log i$  vs.  $\log v$  plots at oxidation and reduction states of Mn<sub>0.33</sub>Co<sub>0.67</sub>N and CoN, respectively; (e) and (f) represent the normalized contribution ratio of capacitive (blue) and diffusion-controlled (green) capacities at different scan rates of Mn<sub>0.33</sub>Co<sub>0.67</sub>N and CoN, respectively; (g) and (h) exhibit capacitive (blue) and diffusion-controlled (green) contributions to charge storage of Mn<sub>0.33</sub>Co<sub>0.67</sub>N and CoN at 0.4 mV s<sup>-1</sup>, respectively.

reduction and oxidation states, respectively, while the  $b$ -values of the  $\text{Mn}_{0.33}\text{Co}_{0.67}\text{N}$  electrode are 0.90, 0.90 and 0.92 at reduction and oxidation states. These  $b$ -values suggest that the charge–discharge process of the  $\text{Mn}_{0.33}\text{Co}_{0.67}\text{N}$  and CoN electrodes includes both conversion reactions and capacitive behavior, and the capacitive behavior is dominant. Among these  $b$ -values, the biggest increase from 0.85 to 0.92 after Mn-doping is observed in oxidation peaks, indicating that the Mn-doping enhances the kinetics of the oxidation process, *i.e.* regeneration of the Co–N bond, as confirmed by the decreased  $E_a$  for Co–N bonding from 113  $\text{kJ mol}^{-1}$  and 96  $\text{kJ mol}^{-1}$  after Mn doping. Such an enhancement of regeneration of Co–N bonds in the present system is schematically illustrated in Fig. 6.

Further quantitative analysis has been carried out to investigate the kinetics of the  $\text{Mn}_{0.33}\text{Co}_{0.67}\text{N}$  and CoN electrodes by separating the diffusion controlled capacity and capacitive capacity. The ratios of Li-ion capacitive contribution can be further quantified by separating the current response  $i$  at a fixed potential  $V$  into capacitive effects (proportional to the scan rate ( $\nu$ ) and diffusion-controlled reactions ( $k_2\nu^{1/2}$ )), according to the following equation:<sup>42</sup>

$$i(\nu) = k_1\nu + k_2\nu^{1/2} \quad (6)$$

By determining both  $k_1$  and  $k_2$  constants, we can distinguish the fraction of the current from surface capacitance and  $\text{Li}^+$  semi-infinite linear diffusion. Fig. 5e and f show the contribution ratios for the capacitive current (blue region) in comparison with the total current. The capacitive capacity keeps increasing along with the increase of voltage scan rates, and pseudocapacitive contribution is more dominant in the total capacity for  $\text{Mn}_{0.33}\text{Co}_{0.67}\text{N}$ , compared with CoN. The capacitive and diffusion-controlled contributions to charge storage at  $0.4 \text{ mV s}^{-1}$  are compared as shown in Fig. 5g and h, it is revealed that the enlarged pseudocapacitive contribution of  $\text{Mn}_{0.33}\text{Co}_{0.67}\text{N}$  mainly locates in the oxidation peaks, further

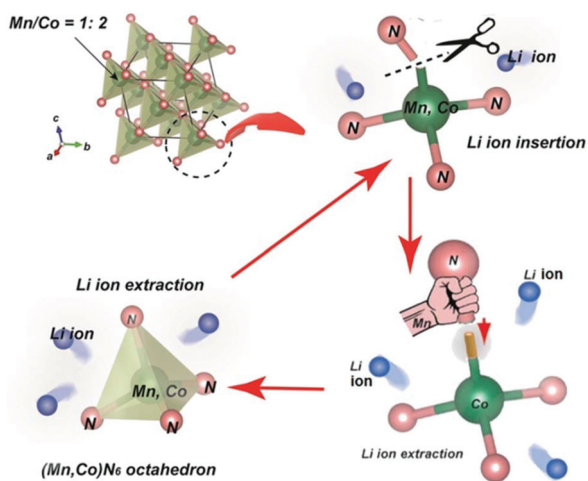


Fig. 6 Schematic illustration of the enhancement of regeneration of Co–N bonds during the lithiation/de-lithiation process by Mn-doping.

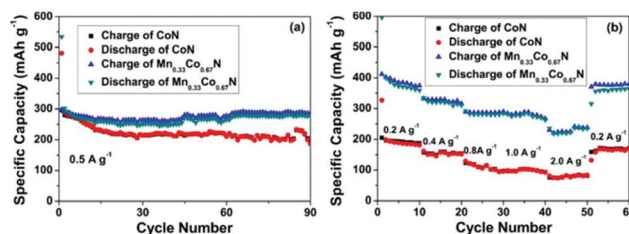


Fig. 7 (a) Comparative cycling performance for sodium ion storage of  $\text{Mn}_{0.33}\text{Co}_{0.67}\text{N}$  and CoN at a current density of  $0.5 \text{ A g}^{-1}$ ; (b) rate properties of the  $\text{Mn}_{0.33}\text{Co}_{0.67}\text{N}$  and CoN at different current densities.

indicating that the Mn-doping facilitates the regeneration kinetics of Co–N bonds.

### 3.6. Extended application of $\text{Mn}_{0.33}\text{Co}_{0.67}\text{N}$ to sodium ion batteries

It is a spontaneous speculation that the expanded lattice, fast formation of Co–N bonds and enhanced structure stability induced by Mn doping can also facilitate sodium ion storage, and could show promising application in sodium storage. If the sodium ion storage performance between CoN and  $\text{Mn}_{0.33}\text{Co}_{0.67}\text{N}$  has a similar feature to the above-mentioned lithium ion storage performance, it will further give another evidence of the positive effect of Mn doping. Indeed, it has been examined as shown in Fig. 7. For the high-rate cycling performance in a sodium ion battery at a current density of  $0.5 \text{ A g}^{-1}$ , as shown in Fig. 6a, the  $\text{Mn}_{0.33}\text{Co}_{0.67}\text{N}$  electrode finally stabilizes at  $277 \text{ mA h g}^{-1}$  after 90 cycles, while the CoN electrode finally stabilizes at  $186 \text{ mA h g}^{-1}$ . The rate capability of the CoN and  $\text{Mn}_{0.33}\text{Co}_{0.67}\text{N}$  electrodes in the range of 0.01–2.80 V is compared at various current densities ( $0.2$ – $2.0 \text{ A g}^{-1}$ ), as shown in Fig. 6b. The  $\text{Mn}_{0.33}\text{Co}_{0.67}\text{N}$  electrode shows high reversible capacities of 361, 318, 281, 279 and  $219 \text{ mA h g}^{-1}$  at current densities of 0.2, 0.4, 0.8, 1.0 and  $2.0 \text{ A g}^{-1}$ , respectively. These intriguing sodium ion storage performances of  $\text{Mn}_{0.33}\text{Co}_{0.67}\text{N}$  electrodes not only give another proof to elucidate the effect of Mn doping, but also suggest the further application of our  $\text{Mn}_{0.33}\text{Co}_{0.67}\text{N}$  anode in  $\text{K}^+$  and  $\text{Mg}^{2+}$  batteries.

## 4. Conclusions

In summary, we firstly report Mn-doped cobalt nitrides ( $\text{Mn}_{0.33}\text{Co}_{0.67}\text{N}$ ) as a novel anode material for LIBs with a high reversible capacity close to  $900 \text{ mA h g}^{-1}$  after 150 cycles at a current density of  $500 \text{ mA g}^{-1}$ , which is superior to  $749 \text{ mA h g}^{-1}$  of undoped CoN. In addition, the most fascinating performance of  $\text{Mn}_{0.33}\text{Co}_{0.67}\text{N}$  is the rate capability, in which 91% of the capacity is maintained when the current density increases ten-fold from  $0.2 \text{ A g}^{-1}$  to  $2.0 \text{ A g}^{-1}$ . This enhanced electrochemical performance is attributed to the fact that Mn doping makes it faster to regenerate Co–N bonds, as evidenced by the calculated apparent ammoniation activation energy ( $E_a$ )

decrease from 113 kJ mol<sup>-1</sup> to 96 kJ mol<sup>-1</sup>. This improved regeneration of Co–N bonds upon conversion reactions is believed to prevent the nitride electrode from a partial loss of charge capacity upon high rate cycling, in turn facilitating the extrinsic pseudocapacitive contribution. Similar features as lithium ion storage performance are observed in sodium ion batteries, which further give another strong proof of the positive effect of Mn doping. Our work quantitatively elucidates the role of Mn doping in the lithium ion storage performance of Mn<sub>0.33</sub>Co<sub>0.67</sub>N, and this quantitative analysis method can be further extended to another cationic doped material based on conversion reactions.

## Conflicts of interest

There are no conflicts to declare.

## Acknowledgements

This work was financially supported by the National Natural Science Foundation of China (No. 51601040, 51701042, 51372040, 51471052, 51571063, U1201241), the Shanghai Rising-Star Program (16QA1400700), and the Science and Technology Commission of Shanghai Municipality (No. 15YF1401300).

## References

- B. Das, M. V. Reddy, G. V. S. Rao and B. V. R. Chowdari, *J. Mater. Chem.*, 2012, **22**, 17505–17510.
- M. S. Balogun, W. T. Qiu, W. Wang, P. P. Fang, X. H. Lu and Y. X. Tong, *J. Mater. Chem. A*, 2015, **3**, 1364–1387.
- T. H. Kim, J. S. Park, S. K. Chang, S. Choi, J. H. Ryu and H. K. Song, *Adv. Energy Mater.*, 2012, **2**, 860–872.
- J. Wu, W. M. Lau and D. S. Geng, *J. Rare Met.*, 2017, **36**, 307–320.
- Z. W. Fu, Y. Wang, X. L. Yue, S. L. Zhao and Q. Z. Qin, *J. Phys. Chem. B*, 2004, **108**, 2236–2244.
- M. V. Reddy, G. Prithvi, K. P. Loh and B. V. Chowdari, *ACS Appl. Mater. Interfaces*, 2014, **6**, 680–690.
- B. Das, M. V. Reddy, P. Malar, T. Osipowicz, G. V. Subba Rao and B. V. R. Chowdari, *Solid State Ionics*, 2009, **180**, 1061–1068.
- Q. Li, L. W. Yin, Z. Q. Li, X. K. Wang, Y. X. Qi and J. Y. Ma, *ACS Appl. Mater. Interfaces*, 2013, **5**, 10975–10984.
- W. Zhang, W. D. Zhou, J. H. Wright, Y. N. Kim, D. W. Liu and X. C. Xiao, *ACS Appl. Mater. Interfaces*, 2014, **6**, 7292–7300.
- R. Baddour-Hadjean and J. P. Pereira-Ramos, *J. Power Sources*, 2007, **174**, 1188–1192.
- J. Cabana, N. Dupré, C. P. Grey, G. Subias, M. T. Caldes, A. T. Maried and M. R. Palacina, *J. Electrochem. Soc.*, 2005, **152**, A2246–A2255.
- B. Das, M. V. Reddy and B. V. Chowdari, *Nanoscale*, 2013, **5**, 1961–1966.
- Y. Song, Y. Cao, J. Wang, Y. N. Zhou, F. Fang, Y. S. Li, S. P. Gao, Q. F. Gu, L. F. Hu and D. L. Sun, *ACS Appl. Mater. Interfaces*, 2016, **8**, 21334–21342.
- Y. Song, Z. L. Chen, Y. M. Li, Q. C. Wang, F. Fang, Y. N. Zhou, L. F. Hu and D. L. Sun, *J. Mater. Chem. A*, 2017, **5**, 9022–9031.
- R. Ma, J. B. Liang, K. Takada and T. Sasaki, *J. Am. Chem. Soc.*, 2011, **133**, 613–620.
- R. Ma, J. B. Liang, X. H. Liu and T. Sasaki, *J. Am. Chem. Soc.*, 2012, **134**, 19915–19921.
- D. L. Chao, C. R. Zhu, P. H. Yang, X. H. Xia, J. L. Liu, J. Wang, X. F. Fan, S. V. Savilov, J. Y. Lin, H. J. Han and Z. X. Shen, *Nat. Commun.*, 2016, **7**, 12122.
- X. Y. Gu, F. L. Wu, B. B. Lei, J. Wang, Z. L. Chen, K. Xie, Y. Song, D. L. Sun, L. X. Sun, H. Y. Zhou and F. Fang, *J. Power Sources*, 2016, **320**, 231–238.
- K. Suzuki, T. Kaneko, H. Yoshida, H. Morita and H. Fujimori, *J. Alloys Compd.*, 1995, 224–232.
- H. Chen, L. F. Hu, X. S. Fang and L. M. Wu, *Adv. Funct. Mater.*, 2012, **22**, 1229–1235.
- Y. T. Li, G. Y. Zhou, F. Fang, X. B. Yu, Q. G. Zhang, L. Z. Ouyang, M. Zhu and D. L. Sun, *Acta Mater.*, 2011, **59**, 1829–1838.
- S. Y. Zheng, F. Fang, G. Y. Zhou, G. R. Chen, L. Z. Ouyang, M. Zhu and D. L. Sun, *Chem. Mater.*, 2008, **20**, 3954–3958.
- F. Fang, Y. T. Li, Y. Song, D. L. Sun, Q. G. Zhang, L. Z. Ouyang and M. Zhu, *J. Phys. Chem. C*, 2011, **115**, 13528–13533.
- X. R. Liu, C. H. Zhao, F. Feng, F. Q. Yu, W. P. Kang and Q. Shen, *RSC Adv.*, 2015, **5**, 7604–7610.
- X. H. Chai, C. S. Shi, E. Z. Liu, J. J. Li, N. Q. Zhao and C. N. He, *Appl. Surf. Sci.*, 2015, **347**, 178–185.
- Q. Sun and Z. W. Fu, *Electrochem. Solid-State Lett.*, 2008, **11**, A233–A237.
- Y. Dong, B. Wang, K. Zhao, Y. Yu, X. Wang, L. Mai and S. Jin, *Nano Lett.*, 2017, **17**, 5740–5746.
- Q. Sun and Z. W. Fu, *Electrochim. Acta*, 2008, **54**, 403–409.
- N. Pereira, L. C. Klein and G. G. Amatucci, *J. Electrochem. Soc.*, 2002, **149**, A262–A271.
- B. Das, M. V. Reddy and B. V. R. Chowdari, *Nanoscale*, 2013, **5**, 1961–1966.
- F. Gillot, J. Oró-Solé and M. R. Palacín, *J. Mater. Chem.*, 2011, **21**, 9997–10002.
- Z. W. Fu, Y. Wang, X. L. Yue, S. L. Zhao and Q. Z. Qin, *J. Phys. Chem. B*, 2012, **108**, 2236–2244.
- B. Das, M. V. Reddy, P. Malar, T. Osipowicz, G. V. Subba Rao and B. V. R. Chowdari, *Solid State Ionics*, 2009, **180**, 1061–1068.
- Q. Sun and Z. W. Fu, *Appl. Surf. Sci.*, 2012, **258**, 3197–3201.
- M. S. Balogun, M. Yu, C. Li, T. Zhai, Y. Liu, X. H. Lu and Y. X. Tong, *J. Mater. Chem. A*, 2014, **2**, 10825–10829.
- J. Liu, S. Tang, Y. K. Lu, G. M. Cai, S. Q. Liang, W. J. Wang and X. L. Chen, *Energy Environ. Sci.*, 2013, **6**, 2691–2697.

- 37 K. S. Park, A. Benayad, D. J. Kang and S. G. Doo, *J. Am. Chem. Soc.*, 2008, **130**, 14930–14931.
- 38 Y. H. Yue, P. X. Han, X. He, K. J. Zhang, Z. H. Liu, C. J. Zhang, S. M. Dong, L. Gu and G. L. Cui, *J. Mater. Chem.*, 2012, **22**, 4938–4943.
- 39 K. Zhang, H. Wang, X. He, *et al.*, *J. Mater. Chem.*, 2011, **21**, 11916–11922.
- 40 G. L. Cui, L. Gu, A. Thomas, L. G. Fu, P. A. Van Aken, M. Antonietti and J. Maier, *ChemPhysChem*, 2010, **11**, 3219–3223.
- 41 I. S. Kim, P. N. Kumta and G. E. Blomgren, *Electrochem. Solid-State Lett.*, 1999, **3**, 493–496.
- 42 R. Wang, S. Wu, Y. Lv and Z. Lin, *Langmuir*, 2014, **30**, 8215–8220.